Journal of Catalysis 394 (2021) 307–315

Contents lists available at ScienceDirect

Journal of Catalysis

journal homepage: www.elsevier.com/locate/jcat

Manganese oxide promoter effects in the copper-catalyzed hydrogenation of ethyl acetate

Rolf Beerthuis [a,1], Nienke L. Visser [a,1], Jessi E.S. van der Hoeven [a,b], Peter Ngene [a], Jon M.S. Deeley [c], Glenn J. Sunley [c], Krijn P. de Jong [a], Petra E. de Jongh [a,*]

[a] Inorganic Chemistry and Catalysis, Debye Institute for Nanomaterials Science, Utrecht University, Universiteitsweg 99, 3584 CG Utrecht, the Netherlands
[b] Soft Condensed Matter, Debye Institute for Nanomaterials Science, Utrecht University, Princetonplein 5, 3584 CC Utrecht, the Netherlands
[c] Applied Chemistry and Physics Centre of Expertise, BP Group Research, Hull Research and Technology Centre, c/o BP Chemicals, Saltend, Hull, United Kingdom

ARTICLE INFO

Article history:
Received 29 June 2020
Revised 1 November 2020
Accepted 2 November 2020
Available online 13 November 2020

Keywords:
Promoter
Manganese
Copper
Heterogeneous catalysis
Hydrogenation
Carbon
Water

ABSTRACT

Supported metal catalysts are widely used in the chemical industry, commonly with added metal oxide promoters to enhance the catalytic performance. Here, we discuss manganese oxide as an efficient promoter for the Cu-based hydrogenation of ethyl acetate; a model hydrogenation reaction. A series of carbon-supported MnO_x-Cu catalysts was prepared with 6 nm MnO_x-Cu particles, while varying the Mn loading between 0 and 33 mol% Mn/(Cu + Mn), without changing the Cu loading or support structure. At temperatures of 180–210 °C and 30 bar pressure, the addition of 11 mol% Mn to Cu gave a 7-fold enhancement in activity, and better catalyst stability. Furthermore, the apparent activation energy decreased from ~100 to 50 kJ mol^{-1}. State-of-the-art characterization allowed to establish a correlation between catalyst structure and performance.

1. Introduction

Supported metal catalysts are widely applied for industrial hydrogenation reactions, with added metal oxide promoters to boost the performance [1–4]. Cu is the metal of choice for the industrial hydrogenation of esters, as it is relatively inexpensive and has a high selectivity towards unsaturated C–O ester bonds while leaving C = C bonds intact [1,5,6]. Promoters are defined as species that exhibit little or no activity alone, but that improve the catalytic performance when added to a catalytically active phase [7]. Already in 1931, chromium oxide was added to promote the Cu-catalyzed hydrogenation of various alkyl esters [8]. The copper chromite catalyst was extensively studied in the following decades and is still used today [1,9,10]. However, carcinogenic Cr^{5+} and Cr^{6+} species may form during catalyst manufacturing and regeneration [11], hence alternative catalysts are desired.

Early studies by Brands *et al.* suggested manganese oxide (MnO_x) as a promising alternative promoter for the Cu-catalyzed hydrogenation of alkyl esters, yet MnO_x promoter effects are little studied [1,12,13]. Metal oxide promoters are generally believed to either change the electronic nature of the active phase, assist in activating reactants and/or stabilizing reaction intermediates [14–16]. Reports exist on MnO_x promotion in other high-pressure hydrogenation reactions, such as Co-catalyzed Fischer-Tropsch synthesis [15,17,18] and Rh [19,20] and Co [21] catalyzed higher alcohols synthesis. However, also for these reactions, the MnO_x promoter effects were mainly studied using metal oxide supports, which typically leads to the formation of stable compounds such as Mn-silicates [15,16,22–24].

In this study we use a chemically inert support, high surface area graphitic carbon, to investigate the intrinsic MnO_x promoter effects. Ethyl acetate (EtOAc) can be produced from synthesis gas [2,13,25–32], and is potentially a key intermediate to produce renewable ethanol [1,26,33,34]. Hence, we chose the hydrogenation of EtOAc [13,35–37] under industrially relevant temperatures and pressure (180–210 °C and 30 bar) as a model reaction. As 6 nm Cu particles give the highest conversion [38], we targeted a MnO_x-Cu particle size of 6 nm, while systematically varying the Mn loading. A combination of STEM-HAADF-EDX and XAS analysis gave insight into the nature of the MnO_x promoter, which allowed us to correlate structural and electronic properties of the promoter to the catalytic performance.

* Corresponding author.
E-mail address: P.E.deJongh@uu.nl (P.E. de Jongh).
[1] Authors contributed equally.

https://doi.org/10.1016/j.jcat.2020.11.003
0021-9517/

2. Experimental methods

2.1. Catalyst preparation

A series of manganese oxide-promoted copper (MnO_x-Cu/C) catalysts was prepared using a high surface area graphitic carbon catalyst support (Graphene nanoplatelets (GNP-500 from XG Sciences), with ~ 500 $m^2\ g^{-1}$ BET surface area and 0.84 mL g^{-1} total pore volume). The carbon support was impregnated until incipient wetness using aqueous solutions of $Cu(NO_3)_2$ and/or $Mn(NO_3)_2$. The impregnated samples were heated to 400 °C, which completely removed the nitrate residues (Fig. S1). The Cu loading was kept constant around 8 wt%, while the Mn loading was varied between 0 and 3.4 wt%, resulting in a mol/mol ratio of Mn/(Cu + Mn) between 0 and 33%. A Cu-free MnO_x/C sample with 7.3 wt% Mn, was prepared using the same synthesis method. Full methods for catalyst preparation are provided in Section S1 of the Supporting Information section.

2.2. Catalyst characterization

Transmission electron microscopy (TEM) was performed on an FEI Tecnai 20 microscope, operated at 200 kV. The catalyst sample was dispersed as a dry catalyst powder, onto a Cu sample grid coated with holey carbon (Agar 300 mesh Cu). The particle size was measured for at least 250 individual particles and on 10 different sample areas. The number-averaged Cu particle sizes (d_n) and surface-averaged Cu particle sizes (d_s), including the standard deviations in the widths of the particle size distributions (σ_{dn} and σ_{ds}), were calculated using the formulas $d_n \pm \sigma_{dn} = \frac{1}{N}\sum_{i=1}^{N} d_i \pm \sqrt{\frac{1}{N}\sum_{i=1}^{N}(d_n - d_i)^2}$ and $d_s \pm \sigma_{ds} = \frac{\sum_{i=1}^{N} d_i^3}{\sum_{i=1}^{N} d_i^2} \pm \sqrt{\frac{1}{N}\sum_{i=1}^{N}(d_s - d_i)^2}$, in which d_i indicates the diameter of the i^{th} particle and N stands for the total count of measured particles. Scanning transmission electron microscopy (STEM) was carried out at an FEI Talos F200X operated at 200 kV. The catalysts sample was dispersed as a dry catalyst powder, onto a Ni sample grid coated with holey carbon (Agar 300 mesh Ni). The images were acquired in high-angle annular dark-field (HAADF) mode. Energy-dispersive X-ray spectroscopy (EDX) mapping was performed to analyse the distribution and amount of the Mn, Cu and C content in the catalyst before and after catalysis.

Powder X-ray diffractometry was performed on a Bruker D8 powder X-ray diffractometer equipped with a Co-$K_{\alpha 1,2}$ radiation source (λ = 1.79026 Å) and a Lynxeye detector. Diffractograms were taken directly after the final step in the synthesis under reductive atmosphere, without exposure to air. The Cu^0 crystallite size was determined by applying the Scherrer equation to the main Cu^0 (2 0 0) diffraction peak at (59.3 °2θ), with a shape factor k of 0.1 [39].

Thermogravimetric analysis was performed on a PerkinElmer Pyris 1 balance, coupled to a Pfeiffer mass spectrometer. The sample (5–10 mg) was measured under Ar flow (20 mL min^{-1}). First, the sample was purged for 30 min at 50 °C, and subsequently heated to 600 °C (5 °C min^{-1}).

Temperature-programmed reduction profiles were measured on a Micromeritics Autochem II ASAP 2920 apparatus, with H_2 consumption quantified using a thermal conductivity detector. Prior to the measurement, the catalysts were dried for 30 min at 120 °C under Ar flow (~1 mL min^{-1} mg^{-1}) and afterwards the temperature was lowered to 50 °C. Next, the reduction profiles were determined by heating the catalyst to 400 °C (2 °C min^{-1}), in a flow of 5 vol% H_2/Ar (~1 mL min^{-1} mg^{-1}). The reduction profiles were base-line corrected and normalized to the amount of Cu per measurement.

X-ray absorption spectroscopy (XAS) data was acquired in transmission mode at the XAFS (BM26A) Dubble beamline at ESRF. The XAS data were recorded near the Mn K-edge (6,340–7,890 eV) or Cu K-edge (8,779–9,629 eV) during separate experiments, using fresh pellets for each measurement. Reference spectra were recorded using commercial Cu foil, Cu_2O, CuO, MnO, Mn_2O_3 and MnO_2 standards. The XAS data was analyzed using Athena data processing software [40].

Further details on STEM-HAADF-EDX analysis, Powder X-ray diffractometry, and XAS analysis and spectra fitting are provided in Section S1.

2.3. Catalytic performance

Catalytic experiments were performed using a gas-phase fixed-bed reactor system, equipped with 16 parallel channels (Flowrence®, Avantium N. V.). The MnO_x-Cu/C catalysts were tested in parallel using the same reactant feed stream. The GHSV for evaporated EtOAC was varied between 2,000 and 17,000 h^{-1}. The effluent gas composition was analysed by on-line gas chromatography at 19 min intervals. To validate that the reaction was not mass transfer limited, we performed measurements with MnO_x-Cu/C catalysts of different granulate size ranges, *i.e.* 75–150 μm, 150–425 μm and 425–630 μm. No substantial differences in conversions were observed, indicating that the reaction was not hindered by internal or external mass transfer limitations. Two reference measurements using either the bare carbon supports or SiC, showed no EtOAc conversion at 210 °C. Further details on the catalytic experiments, and calculations of TOF, standard deviations, apparent activation energies and kinetic studies are provided in the Supporting Information.

3. Results and discussion

3.1. Structural properties of MnO_x-Cu catalysts

Transmission electron micrographs (TEM) and particle size distributions for two representative MnO_x-Cu/C catalysts are shown in Fig. 1a and 1b. The characterization for the full series of catalysts is provided in Section S2. In all cases, bright-field TEM analysis showed highly dispersed nanoparticles, mainly situated on the edge positions of the graphitic carbon sheets. Broad Cu^0 diffraction peaks were observed in the powder X-ray diffractograms (XRD) for all reduced MnO_x-Cu/C catalysts (Fig. 1c). A Cu-free sample with 7.3 wt% Mn (100_MnO_x/C) had MnO_x particles of approximately 2.3 nm in size (Fig. S2g). None of the samples showed crystalline manganese oxide phases by XRD analysis. Table 1 shows that the MnO_x-Cu particle size and Cu^0 crystallite size consistently remained around 5 to 6 nm, even upon increasing the Mn loading from 0 to 3.4 wt%, while keeping the Cu loading around 8 wt%. While heating the impregnated catalyst precursors to 230 °C was sufficiently high to achieve precursor decomposition, heating to 400 °C was essential to obtain $CuMnO_x$ particles with a particle size of around 6 nm [38]. The catalysts were denoted here as X_MnO_x-Cu/C, in which X represents the Mn loading as mol% Mn/(Cu + Mn).

The size and location of the MnO_x promoter were investigated by energy-dispersive X-ray (EDX) analysis. All fresh catalyst showed distinct Cu nanoparticles of around 5 nm (Figs. S2 and S3). With increasing Mn loadings, the MnO_X promoter appeared to accumulate as small MnO_x islands in close proximity to the Cu nanoparticles, but additionally some highly-dispersed MnO_x was detected. The local elemental composition was in good agreement with the bulk loadings: 32 mol% Mn for 33_MnO_x-Cu/C and 10 mol % Mn for 11_MnO_x-Cu/C (Figs. S4 and S5). The local compositions hence corroborated the bulk loadings, and showed homogeneous

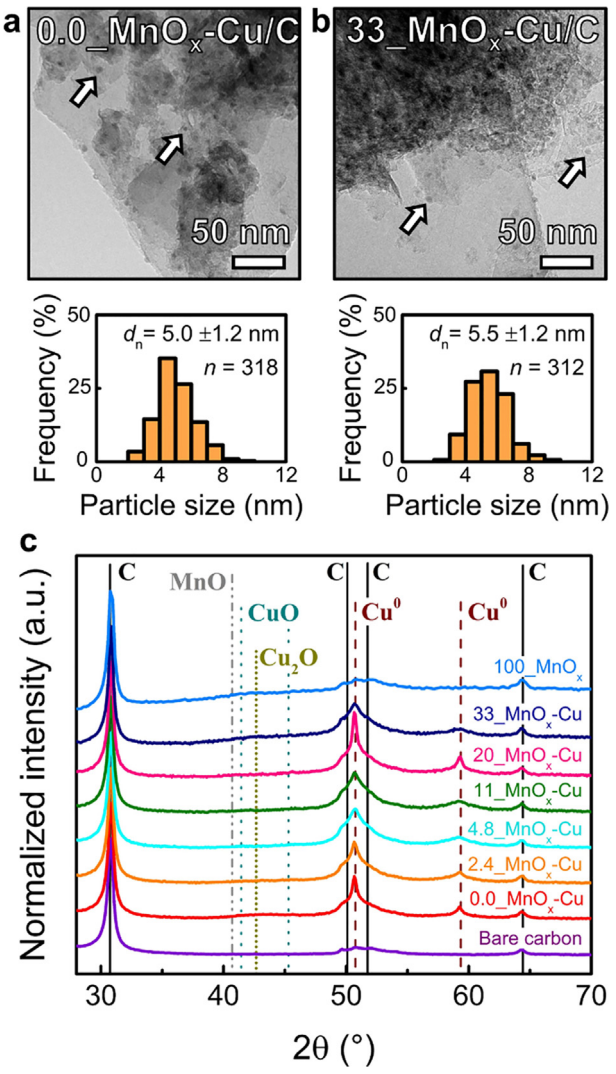

Fig. 1. Transmission electron micrographs with arrows indicating several representative nanoparticles, with corresponding particle size distributions and number-averaged MnO_x-Cu particle sizes (d_n), as determined by counting n number of particles, displayed for (a) 0.0_MnO_x-Cu/C and (b) 33_MnO_x-Cu/C catalysts; (c) Powder X-ray diffractograms of reduced Cu/C, MnO_x-Cu/C and MnO_x/C samples and the bare graphitic carbon support.

Table 1
Structural properties for the carbon-supported MnO_x and/or Cu samples.

Catalyst	Cu (wt%)	Mn (wt%)	XRD d^0_{Cu} (nm)	TEM $d_n \pm \sigma_{dn}$ (nm)[a]	TEM $d_s \pm \sigma_{ds}$ (nm)[a]
0_MnO_x-Cu/C	8.7	0	6.9	5.0 ± 1.2	5.6 ± 1.3
2.4_MnO_x-Cu/C	8.7	0.2	6.3	5.3 ± 1.2	5.8 ± 1.3
4.8_MnO_x-Cu/C	8.4	0.4	6.3	5.1 ± 1.3	5.7 ± 1.4
11_MnO_x-Cu/C	8.5	0.9	5.6	5.6 ± 1.3	6.2 ± 1.5
20_MnO_x-Cu/C	8.4	1.8	5.4	5.5 ± 1.7	6.7 ± 2.0
33_MnO_x-Cu/C	7.9	3.4	6.3	5.5 ± 1.2	6.0 ± 1.3
100_MnO_x/C	0	7.3	–	2.3 ± 1.0	3.4 ± 1.6

(**a**) Number-averaged MnO_x-Cu particle size (d_n), surface-averaged MnO_x-Cu particle size (d_s) and standard deviations in the width of the particle size distributions (σ_{dn} and σ_{ds}).

Cu and Mn distributions throughout the catalysts. Fine-tuning the synthesis parameters uniquely allowed us to obtain similar MnO_x-Cu particle sizes over a wide range of Mn loadings.

3.2. Impact of Mn loading on catalyst performance

An overview of the EtOAc conversion as a function of time and at different temperatures, is given in Fig. 2a and 2b. The conversion typically increased during the first 30 h on stream (at 180 °C). Initial changes in activity are common for Cu-catalyzed hydrogenation reactions. The 33_MnO_x-Cu/C catalyst did not show particle growth during catalysis, and therefore the initial increase in conversion was not ascribed to particle growth. The activation behavior is likely caused by nanoparticle surface restructuring and equilibration of the surface adsorbate composition [41–43]. The Cu-free 100_MnO_x/C sample showed no significant EtOAc conversion, but the presence of MnO_x increased the EtOAc conversion for all Cu-based catalysts. For example, the EtOAc conversion after 30 h at 180 °C increased from 2.3% for un-promoted 0.0_MnO_x-Cu/C up to 12.7% for 11_MnO_x-Cu/C. Interestingly, the conversion decreased after 60 h for catalysts with $\geq$ 11 mol% Mn, reflecting deactivation. The presence of a modest amount of MnO_x (<11 mol% Mn) hence improved both the activity and stability.

The apparent activation energies (E_a, Fig. 2c) were calculated from the slope of a linearly fit through the ln(r) values in the Arrhenius plots (Fig. S6). Herein, the reaction rate r was defined as $mmol_{EtOH}\ g_{Cu}^{-1} h^{-1}$. The EtOAc conversions were all below 50% and hence well below the equilibrium conversion which was calculated to be > 93% at 180–210 °C. To minimize the influence of the initial activation behavior during the first 30 h on stream (180 °C), we only used the reaction rates between 30 and 150 h on stream, including the final isothermal stage at 180 °C (120–150 h). The reaction rates were calculated from the final conversions at each temperature stage, which takes into account that the conversions at different temperatures were also influenced by (de-)activation over time on stream. The fits for the E_a calculations were shown in Fig. 2b as dashed lines. For completeness, in Fig. S7 a comparison was made between the E_a values using either the initial or the final isothermal stage at 180 °C, which shows the same trend in both cases. The E_a decreased from 104 kJ mol^{-1} for 0.0_MnO_x-Cu/C to 54 kJ mol^{-1} for 11_MnO_x-Cu/C. For Mn loadings above 11 mol%, the E_a remained approximately constant. The E_a values in this study are in good agreement with reported values of 119 kJ mol^{-1} for macroscopic Cu [13], 94–107 kJ mol^{-1} for un-promoted supported Cu [37] and 74 kJ mol^{-1} for ZrO_2-promoted Cu [36]. The reduced E_a here indicate that the MnO_x promoter alters the nature of the active catalytic site for the rate-determining step. The relationship between Mn loading and turn-over frequency (TOF; at 180 °C) is shown in Fig. 2d. The initial TOF increased approximately 7-fold from $1.2*10^{-3}$ s^{-1} for 0.0_MnO_x-Cu/C to $7.7*10^{-3}$ s^{-1} for 11_MnO_x-Cu/C. However, increasing the Mn loading above 11 mol% Mn did not enhance the initial TOF but even slightly lowered it. By comparison, Wang *et al.* reported that a maximum TOF for MeOAc hydrogenation was obtained using around 10 mol% Zn/(Cu + Zn) for SiO_2-supported Cu catalysts [44].

The MnO_x-Cu/C catalysts in our study were significantly more active than (promoted) Cu catalysts in literature. For example, Santiago *et al.* reported a TOF of $2.7*10^{-3}$ s^{-1} at 250 °C for Cu/SiO_2 [28], and Lu *et al.* reported TOF values around $1.1*10^{-3}$ s^{-1} at 280 °C for Zn-promoted Cu catalysts supported on SiO_2, Al_2O_3 and ZrO_2 [45], while we measured TOF between 1.2 and $7.7*10^{-3}$ s^{-1} at a lower temperature of 180 °C. An explanation for our higher TOF may be the use of a high purity EtOAc reactant, with approximately 50 ppm of water, as determined by Karl Fischer titration. To investigate the influence of water in the EtOAc feed, we incrementally increased the concentration during an experiment at 200 °C and 30 bar (Fig. S8). Increasing the water concentration in the liquid EtOAc feed from 50 to 400 ppm led to a 3-fold decrease in conversion for the 11_MnO_xCu/C catalyst, while for the unpromoted Cu/C

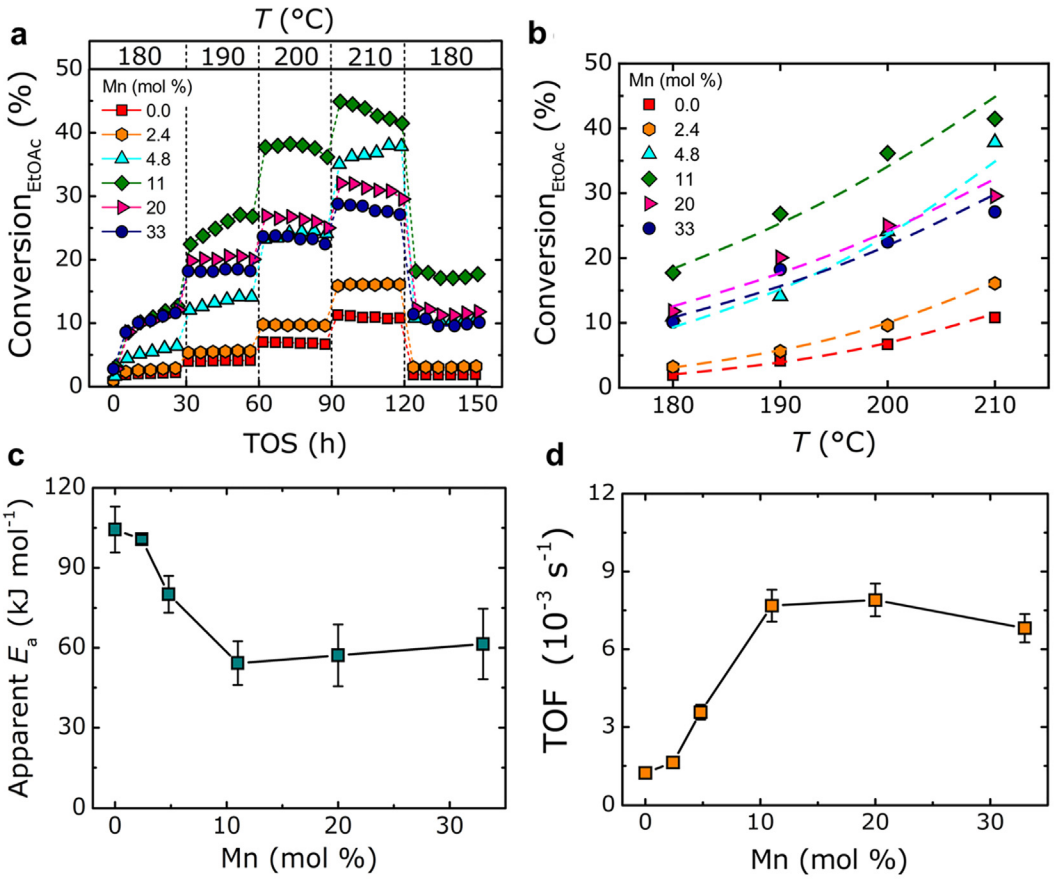

Fig. 2. Catalytic performance for MnO_x-Cu/C catalysts with varying Mn loading between 0 and 33 mol%; EtOAc conversion as a function of (**a**) time on stream (TOS) at different temperatures, and (**b**) final conversions at temperature stages (180–210 °C) between 30 and 150 h on stream (using the final isothermal stage at 180 °C). The dashed lines indicate the fits used for the calculation of the apparent activity energies (E_a); (**c**) Values of E_a as a function of Mn loading; (**d**) Turn-over frequencies (TOF) at 180 °C, at t = 30 h and based on the particle size of the fresh catalyst. Reaction conditions: H_2:He:EtOAc = 10:1:1 vol%, 50 ppm water in EtOAc feed, 180–210 °C, 30 bar and GHSV between 6,200–7,200 h^{-1}.

catalyst nearly all activity was lost (Fig. 3). The almost immediate loss of conversion was ascribed to the strong adsorption of water on the catalyst surface, inhibiting the hydrogenation reaction. For the promoted Cu/C catalysts the conversion of the promoted Cu/C catalysts remained much higher than for the unpromoted Cu/C catalyst when returning to the initial water concentration of 50 ppm, indicating that the surface inhibition was largely reversible in the presence of MnO_x. The particle size of the unpromoted Cu/C catalyst increased from 5.0 ± 1.2 to 16.4 ± 5.7 nm, hence causing irreversible loss of activity. In contrast, the 33_MnO_x-Cu/C catalyst showed only particle growth from 5.5 ± 1.2 to 6.2 ± 1.5 nm (Fig. S9). The MnO_x promoter hence mitigated the irreversible catalyst deactivation through water-induced particle growth.

Remarkably, the selectivity towards ethanol was >99.5% for all MnO_x-Cu/C catalysts between 180 and 210 °C (up to 40% conversion, see Fig. 4). The selectivity decreased with increasing EtOAc conversion (and increasing reaction temperature). However, the presence of Mn improved the ethanol selectivity when comparing at similar EtOAc conversions, with > 99.9% for the 11_MnO_x-Cu/C catalyst at 25% EtOAc conversion. Ethane was observed as the main by-product (Fig. S10), with only traces of acetic acid and acetaldehyde. The selectivity for MnO_x-Cu/C was significantly higher than reported in literature for supported Cu-based catalysts, which were typically < 95% under similar reaction conditions [3,26,28,36,45]. The lower literature values were probably caused by acidic or basic surface groups on the metal oxide supports [36], which were absent on our carbon support.

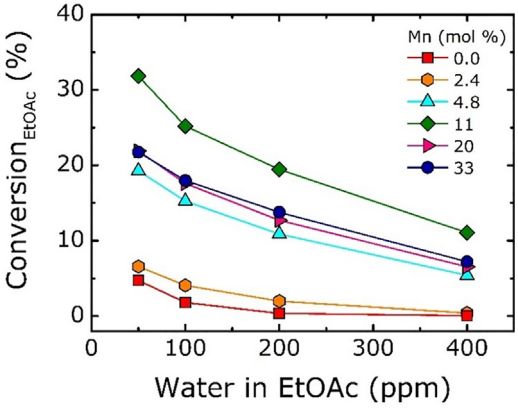

Fig. 3. EtOAc conversion as a function of water concentration in the EtOAc feed. Conversions determined after 45 h at each stage of varied water concentrations. Reaction conditions: H_2:He:EtOAc = 10:1:1 vol%, 50–400 ppm water in EtOAc feed, 200 °C, 30 bar and GHSV between 6,200–7,200 h^{-1}.

3.3. Nature of the MnO_x promoter

The observed phenomena raise the question which MnO_x species are responsible for the enhanced activity, and how the nature of the Cu particles is affected under reaction conditions (H_2 flow, 180–210 °C). To address these questions, we studied the Cu and Mn oxidation states upon reduction. The MnO_xCu/C catalysts

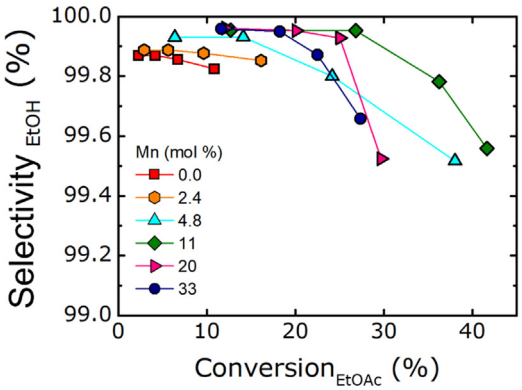

Fig. 4. Ethanol selectivity as a function of EtOAc conversion, for MnO_x-Cu/C catalysts with Mn loading between 0 and 33 mol% Mn/(Cu + Mn), prepared using graphitic carbon as support. Reaction conditions: H_2:He:EtOAc = 10:1:1 vol%, 50 ppm water in EtOAc feed, 180–210 °C, 30 bar and GHSV between 6,200–7,200 h^{-1}.

showed H_2 consumption between 100 and 250 °C, corresponding to the reduction of CuO to Cu_2O and subsequently to Cu^0 (Fig. S11) [46–50]. For the Cu-free MnO_x/C sample, the H_2 consumption showed a broad peak between 300 and 600 °C, indicating MnO_x reduction [51]. For all MnO_x-promoted Cu/C catalysts, the H_2 consumption was larger than H_2:Cu = 1:1 mol/mol (Table S3). Moreover, the peak between 300 and 600 °C was less pronounced for MnO_xCu than for MnO_x alone, which likely results from a lower average Mn oxidation state. These results suggest that MnO_x, and the Cu are in close proximity, and that Cu facilitated the partial reduction of MnO_x below 250 °C [1,12,24,45,52].

In situ X-ray absorption spectroscopy (XAS) was applied to investigate the Cu and Mn oxidation states before and after reduction. The Cu K-edge absorption energies for the catalysts after synthesis (passivated) were consistently located between the Cu^+ and Cu^{2+} references within 8,970 to 9,010 eV (Fig. S12), corresponding to average an average Cu oxidation state of 1.3–1.6 (Table S3). After *in situ* reduction (1 h at 250 °C, 4 vol% H_2/He flow) all spectra were similar to the Cu foil reference (Fig. 5a). A close overlap between the fitted and measured spectra, indicates complete reduction to Cu^0, irrespective of the Mn loading (Fig. S13). The Cu–Cu coordination number (CN_{Cu-Cu}) ranged from 10.2 to 11.3 for all MnO_x-Cu/C catalysts, corroborating the size range of 5–6 nm as measured by TEM and XRD analysis (Table S3) [53–55]. The CN_{Cu-Cu} was slightly higher for the un-promoted Cu/C catalyst (11.3) compared to MnO_x-Cu/C catalysts (10.2–10.8), suggesting a slightly larger Cu particle size.

The Mn K-edge absorption energies for both the MnO_x-Cu/C catalysts after synthesis (passivated, Fig. S12) and after reduction were consistently located between the Mn^{2+} and Mn^{3+} references (Fig. 5c). For the passivated catalysts, both the Mn–O (R = 1.0–1.5 Å) and Mn–Mn (R = 2.5–3.0 Å) scattering intensities increased with increasing Mn loadings, suggesting Mn accumulation as MnO_x particles. However, the MnO_x particle size analysis was hampered due to overlapping signals for Mn^{2+} and Mn^{3+} oxides (Fig. 5d). Upon reduction at 250 °C, all Mn (pre-)edge absorption energies shifted to lower values. The average Mn oxidation state decreased from 2.3 to 2.9 to 2.2–2.5, in line with the partial reduction of MnO_x as observed by H_2-TPR (Table S3). Interestingly, the Mn oxidation state for the reduced MnO_x-Cu/C catalysts increased from 2.2 to 2.5 with increasing Mn loading from 2.4 to 11 mol%, yet remained approximately 2.5 when further increasing in the Mn loading (Fig. 6). This suggests that at low MnO_x loadings, when the promotion is most effective, the Mn is in an oxidation state closer to 2+ after reduction and closely associated with the Cu. At Mn loadings above 11 mol%, the additional MnO_x with a Mn oxidation state closer to 3+ after reduction did not significantly contribute to further promotion.

Metal oxide promoters are generally believed to either change the electronic nature of the active metal phase, or assist in activating reactants and/or stabilizing reaction intermediates at the interface [14,15,17,20,44]. Our XAS analysis did not provide any evidence for an Cu oxidation state other than Cu^0 for both promoted and unpromoted catalysts. Further mechanistic insight into the promoter effect was obtained from a series of measurements of the EtOAc hydrogenation reaction rate as a function of the partial pressures of H_2, EtOAc and H_2O, to determine the reaction orders (Fig. S14). Cu catalysts with and without MnO_x were tested, under steady state operation and at similar conversion levels (~12%). The observed reaction orders in H_2 were 0.97 ± 0.04 for unpromoted Cu/C and 0.78 ± 0.11 for 33_MnO_x-Cu/C. The near first order dependency in H_2 concentration suggests a low hydrogen surface coverage, for both promoted and unpromoted catalysts, indicating that the dissociative adsorption of hydrogen is the limiting factor for this reaction. Our findings hence corroborate studies in literature which report that the surface hydrogenation of the acyl reaction intermediates is the rate-determining step in alkyl ester hydrogenation [13,28,36]. The MnO_x promoter appeared to slightly increase the surface coverage by H_2, improving the reaction rate. The reaction orders in EtOAc were 0.05 ± 0.01 for unpromoted Cu/C and 0.14 ± 0.03 for 33_MnO_x-Cu/C. The near zeroth orders in EtOAc concentration for both catalysts are in good agreement with kinetic studies in literature, and suggests a Cu surface saturation by strongly adsorbed (dissociated) EtOAc species [13,35–37]. The reaction orders in H_2O were −2.24 ± 0.24 for unpromoted Cu/C and −0.52 ± 0.11 for 33_MnO_x-Cu/C. The H_2O orders for both catalysts were negative, clearly showing the inhibiting effect of increased H_2O concentrations. The presence of 4.8 mol% or above of MnO_x gave a reaction order closer to zero, hence mitigating the reversible catalyst deactivation.

3.4. Evolution of catalyst structure and activity

Particle growth generally is a major deactivation mechanism for nanoparticulate Cu catalyzed hydrogenation reactions, as the active surface area per gram of Cu decreases with increasing particle size [56–59]. However for Cu particles smaller than 10 nm, the loss of surface area is compensated by a gain in specific activity [38]. Hence, particle growth only strongly decreases the overall conversion for particles of 10 nm and larger, when the Cu particle size effects become negligible.

The MnO_x-Cu particle sizes by TEM were compared for the fresh catalysts after synthesis and used catalyst after 150 h on stream at 180–210 °C (Fig. 7a, S15 and S16). The Cu particle size of the unpromoted 0.0_MnO_x-Cu/C catalyst increased from 5.0 nm to 9.7 nm. The presence of MnO_x limited the particle growth, *e.g.* from 5.1 nm to 5.5 nm for the 4.8_MnO_x-Cu/C catalyst. The MnO_x promoter hence not only enhanced the conversion and selectivity, but also limited Cu particle growth during catalysis, with 5–10 mol % Mn being sufficient to achieve this effect.

The evolution of activity was evaluated by comparing initial and final TOF values (Fig. 7b). In absence of Mn, the TOF for the unpromoted 0.0_MnO_x-Cu/C catalyst increased 2-fold from $1.2*10^{-3}$ s^{-1} to $2.1*10^{-3}$ s^{-1}, while the Cu particle size increased from 5.0 to 9.7 nm. The increase in TOF was ascribed to a higher intrinsic activity for increasing particle size up to 10 nm [38]. In the presence of 2.4–11 mol% Mn, the TOF slightly increased during the reaction, while it slightly decreased for catalysts with ≥ 20 mol% Mn. Under isothermal reaction conditions (during 225 h at 200 °C, see Fig. S17), a slower activation was observed for the catalysts with 2.4 and 4.8 mol% Mn, while deactivation dominated for

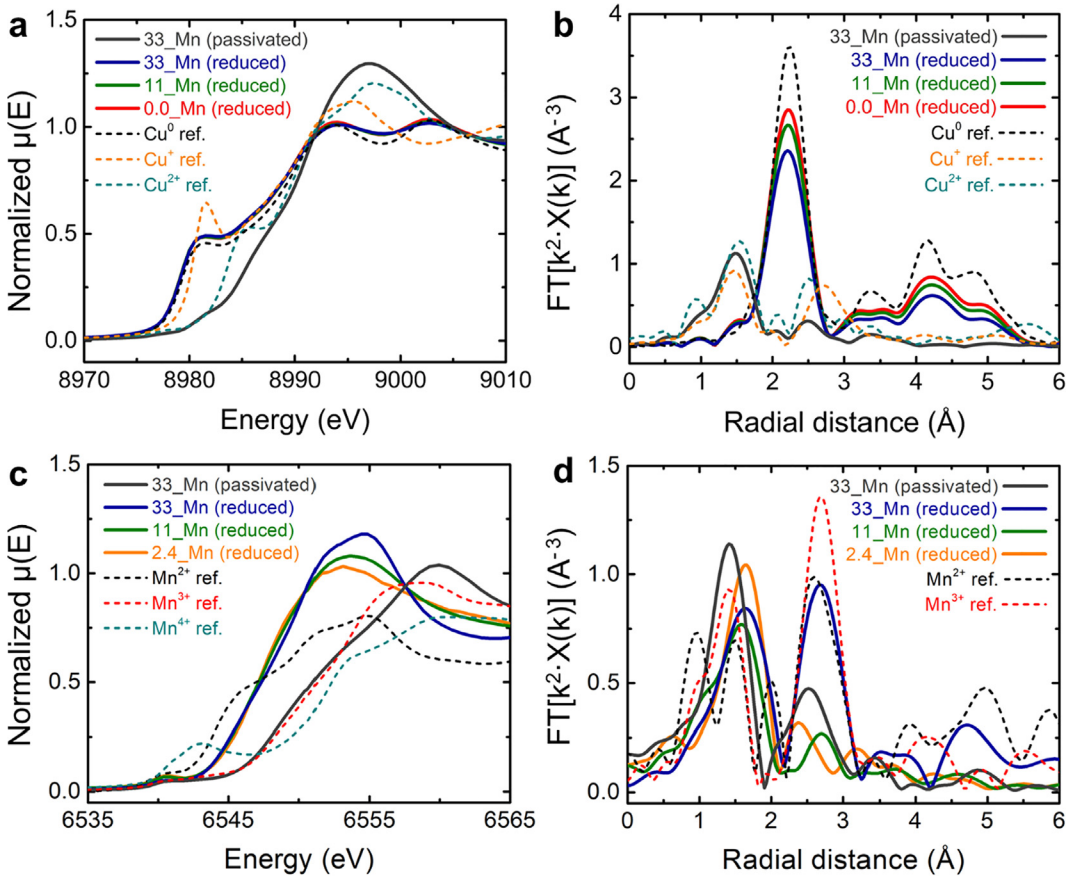

Fig. 5. X-ray absorption spectra for several representative MnO_x-Cu/C catalysts after synthesis (passivated) and after reduction for 1 h at 250 °C under 4 vol% H_2/He flow (reduced), including reference spectra (dashed lines); (**a**) normalized absorption near the Cu K-edge (**b**) corresponding Fourier transform (k^2 weighted); (**c**) normalised absorption near the Mn K-edge; (**d**) corresponding Fourier transform (k^2-weighted).

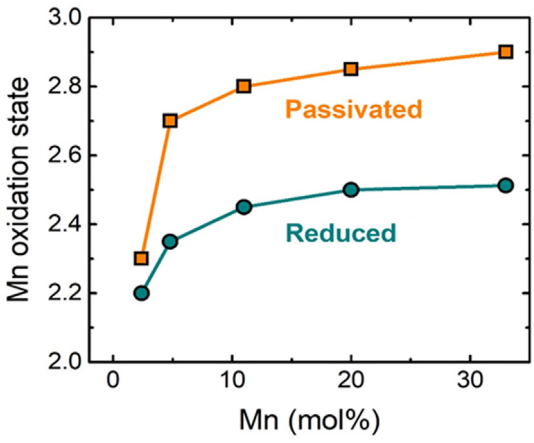

Fig. 6. Average Mn oxidation state as a function of Mn loading, for MnO_x-Cu/C catalysts after synthesis (passivated) and after reduction (1 h at 250 °C, 4 vol% H_2/He flow), as determined from the linear correlation between Mn oxidation state values and the energy of the pre-edge feature between 6,535 to 6,545 eV in the XANES.

loadings > 11 mol% Mn. These changes were not caused by changes in particle size, which were small in the presence of MnO_x (Fig. 7a), hence we ascribed them to changes in the oxidation state and/or distribution of the MnO_x promoter during catalysis [4,12,15,16,22].

To evaluate the changes in MnO_x structure over time, we analyzed with STEM-HAADF-EDX the Mn distribution for the fresh 33_MnO_x-Cu/C catalyst after synthesis and for the used catalyst after 150 h catalysis at 180–210 °C (Fig. 8). For the fresh catalyst, distinct MnO_x nanoparticles were observed in close proximity to the Cu nanoparticles. For the used catalyst, the MnO_x promoter was spread more evenly over the carbon support, suggesting that re-dispersion of surface-mobile MnO_x species occurred during catalysis. Quantification of the Mn concentration showed approximately 33 mol% Mn/(Cu + Mn) before and after catalysis, indicating that no leaching occurred. The spreading of MnO_x was even more clearly seen for the Cu-free 100_MnO_x/C sample after exposure to reaction conditions (Fig. S18). The EDX analysis showed that the used sample contained significantly smaller MnO_x particles (1.2 ± 0.3 nm) than the fresh sample (2.3 ± 1.0 nm). Our results show that, irrespective of Cu being present or not, the MnO_x promoter readily spreads over the support under reaction conditions. The presence of EtOAc and traces of water (~50 ppm) likely played a role in forming surface-mobile Mn species at elevated temperatures. The presence of 20 mol% Mn corresponds to 1.4 theoretical monolayers on the Cu particles (Table S2). As also some MnO_x does not stay in contact with the Cu but instead spreads over the carbon support, it is evident only a fraction of the Cu surface is covered by MnO_x for $\leq$ 11 mol% Mn. These findings demonstrate the importance of a balanced Mn loading for optimum catalytic performance of the Cu nanoparticles.

4. Conclusions

A series of well-defined MnO_x-Cu catalysts was prepared *via* co-impregnation, using high surface area graphitic carbon as the catalyst support. Tuning the synthesis parameters allowed us to keep the MnO_x-Cu particle size constant around 6 nm, while varying the

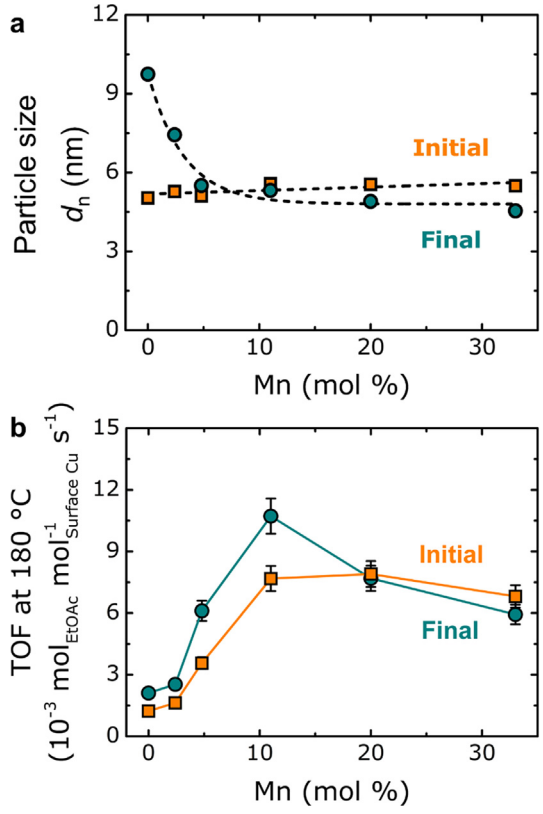

Fig. 7. (**a**) Particle sizes by TEM for the fresh MnO_x-Cu/C catalysts after synthesis (initial, orange squares) and used catalysts after 150 h catalysis at 180–210 °C (final, cyan circles) as a function of MnO_x loading; (**b**) Turn-over frequencies (TOF, at 180 °C) are given both after 30 h and correlated to the initial particle size (orange squares) and after 150 h and correlated to the final particle size (cyan circles). Error bars indicate the relative standard deviation. Reaction conditions: H_2:He: EtOAc = 10:1:1 vol%, 50 ppm water in EtOAc feed, 180–210 °C, 30 bar and GHSV between 6,200–7,200 h^{-1}.

Mn loading between 0 and 33 mol% Mn/(Cu + Mn). The methodology for catalyst preparation may be relevant for a wide range of metals and promoters. The addition of 11 mol% Mn to Cu, induced a 7-fold increase in TOF and a concomitant decrease in the apparent activation energy from 104 to 54 kJ mol^{-1}. Water in the EtOAc feed strongly decreased the catalytic activity, while the MnO_x promoter enhanced the resistance against water-induced decrease in conversion. The selectivity towards ethanol was > 99.5%, much higher than reported in literature. During catalysis the MnO_x re-dispersed and especially for MnO_x loadings >11 mol%, a fraction with a somewhat higher Mn oxidation state was not in contact with the Cu, and did not contribute to a further increase in activity. In our study 11 mol % Mn provided an optimum combination of high activity, selectivity and stability.

Declaration of Competing Interest

The authors declare that they have no known competing financial interests or personal relationships that could have appeared to influence the work reported in this paper.

Acknowledgements

The authors thank Jan Willem de Rijk, Remco Dalebout, Neil Sainty and Roy Partington for support in catalytic experiments, Christa C. M. Oversteeg, Fei Chang, Herrick van Schaink, Ad van der Eerden and Alessandro Longo for their contributions to the X-ray absorption spectroscopy measurements and data processing. The authors acknowledge the awarded beamtime on the Dubble beamline 26A at Synchrotron ESRF under proposal number 26-11 1175. BP was gratefully acknowledged for funding RB, ERC (grant number ERC-2014-CoG-648991) for additional funding for PEdJ, and ERC (grant number ERC-AG338846) for additional funding for KPdJ and supporting the transmission electron microscopy facilities.

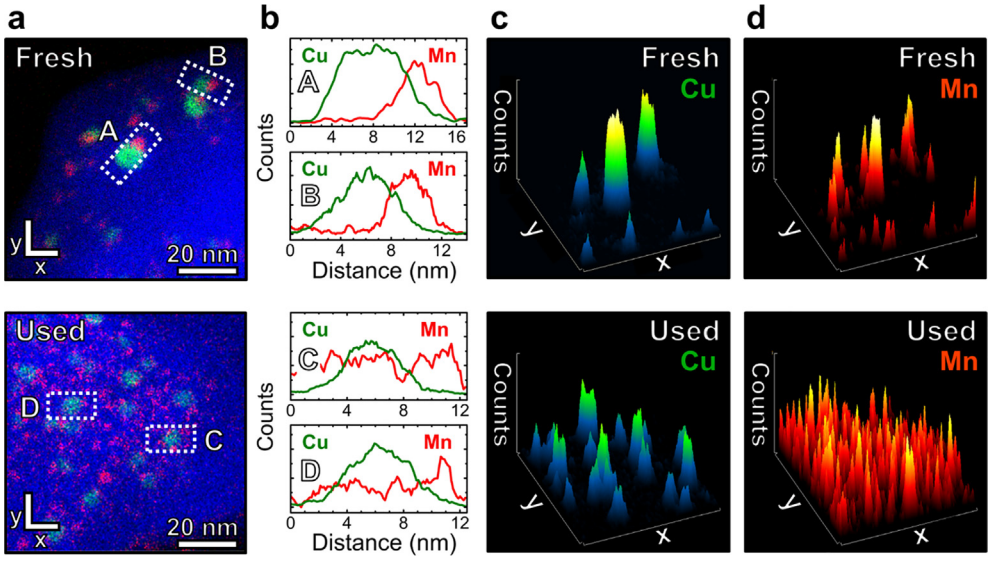

Fig. 8. STEM-HAADF-EDX analysis for the fresh 33_MnO_x-Cu/C catalyst after synthesis and used catalyst after 150 h catalysis at 180–210 °C. (**a**) 2-dimensional EDX maps showing the elemental distributions for carbon (blue), Cu (green) and Mn (red), including regions A–D for line scan analysis (dashed white boxes); (**b**) Cu and Mn line scan analysis, displaying EDX intensity over the length of the indicated regions (A–D); (**c** and **d**) 3-dimensional intensity plots in Cu and Mn EDX signals, acquired over the x,y-planes as indicated in the EDX maps.

Appendix A. Supplementary material

Supplementary data to this article can be found online at https://doi.org/10.1016/j.jcat.2020.11.003.

References

[1] D.S. Brands, E.K. Poels, A. Bliek, Ester hydrogenolysis over promoted Cu/SiO2 catalysts, Appl. Catal. A 184 (1999) 279–289.
[2] F.T. Van de Scheur, L.H. Staal, Effects of zinc addition to silica supported copper catalysts for the hydrogenolysis of esters, Appl. Catal. A 108 (1994) 63–83.
[3] Y.-M. Zhu, L. Shi, Zn promoted Cu–Al catalyst for hydrogenation of ethyl acetate to alcohol, J. Ind. Eng. Chem. 20 (2014) 2341–2347.
[4] C. Ye, C. Guo, C. Sun, Y. Zhang, Effect of Mn doping on the activity and stability of Cu–SiO2 catalysts for the hydrogenation of methyl acetate to ethanol, RSC Adv. 6 (2016) 113796–113802.
[5] F.T. Van de Scheur, B. van der Linden, M.C. Mittelmeijer-Hazeleger, J.G. Nazloomian, L.H. Staat, Structure-activity relation and ethane formation in the hydrogenolysis of methyl acetate on silicasupported copper catalysts, Appl. Catal. A 111 (1994) 63–77.
[6] M.B. Gawande, A. Goswami, F.-X. Felpin, T. Asefa, X. Huang, R. Silva, X. Zou, R. Zboril, R.S. Varma, Cu and Cu-based nanoparticles: synthesis and applications in catalysis, Chem. Rev. 116 (2016) 3722–3811.
[7] G. Ertl, H. Knözinger, J. Weitkamp, Handbook of Heterogeneous Catalysis, Wiley, 2008.
[8] H. Adkins, K. Folkers, The catalytic hydrogenation of esters to alcohols, JACS 53 (1931) 1095–1097.
[9] T. Turek, D.L. Trimm, N.W. Cant, The catalytic hydrogenolysis of esters to alcohols, Catal. Rev. 36 (1994) 645–683.
[10] R. Rao, A. Dandekar, R.T.K. Baker, M.A. Vannice, Properties of copper chromite catalysts in hydrogenation reactions, J. Catal. 171 (1997) 406–419.
[11] S.A. Katz, H. Salem, The toxicology of chromium with respect to its chemical speciation: A review, J. Appl. Toxicol. 13 (1993) 217–224.
[12] D.S. Brands, E.K. Poels, A. Bliek, The relation between pre-treatment of promoted copper catalysts and their activity in hydrogenation reactions, in: J. W. Hightower, W. Nicholas Delgass, E. Iglesia, A.T. Bell (Eds.) Stud. Surf. Sci. Catal., Elsevier, 1996, pp. 1085–1094.
[13] P. Claus, M. Lucas, B. Lücke, T. Berndt, P. Birke, Selective hydrogenolysis of methyl and ethyl acetate in the gas phase on copper and supported Group VIII metal catalysts, Appl. Catal. A 79 (1991) 1–18.
[14] A. Yin, X. Guo, W.-L. Dai, K. Fan, The nature of active copper species in Cu-HMS catalyst for hydrogenation of dimethyl oxalate to ethylene glycol: new insights on the synergetic effect between Cu0 and Cu+, J. Phys. Chem. C 113 (2009) 11003–11013.
[15] G.R. Johnson, S. Werner, A.T. Bell, An investigation into the effects of Mn promotion on the activity and selectivity of Co/SiO2 for Fischer-Tropsch synthesis: evidence for enhanced CO adsorption and dissociation, ACS Catal. 5 (2015) 5888–5903.
[16] F. Morales, D. Grandjean, A. Mens, F.M.F. de Groot, B.M. Weckhuysen, X-ray absorption spectroscopy of Mn/Co/TiO2 Fischer−Tropsch catalysts: relationships between preparation method, molecular structure, and catalyst performance, J. Phys. Chem. B 110 (2006) 8626–8639.
[17] Y. Xiang, N. Kruse, Tuning the catalytic CO hydrogenation to straight- and long-chain aldehydes/alcohols and olefins/paraffins, Nat. Commun. 7 (2016) 13058.
[18] H.M. Torres Galvis, K.P. de Jong, Catalysts for production of lower olefins from synthesis gas: a review, ACS Catal. 3 (2013) 2130–2149.
[19] Z. Xie, B. Frank, X. Huang, R. Schlögl, A. Trunschke, Higher alcohol synthesis over Rh catalysts: conditioning of Rh/N-CNTs by Co and Mn entrapped in the support, Catal. Lett. 146 (2016) 2417–2424.
[20] N. Yang, J.S. Yoo, J. Schumann, P. Bothra, J.A. Singh, E. Valle, F. Abild-Pedersen, J. K. Nørskov, S.F. Bent, Rh-MnO interface sites formed by atomic layer deposition promote syngas conversion to higher oxygenates, ACS Catal. 7 (2017) 5746–5757.
[21] J. Paterson, M. Peacock, R. Purves, R. Partington, K. Sullivan, G. Sunley, J. Wilson, Manipulation of Fischer-Tropsch synthesis for production of higher alcohols using manganese promoters, ChemCatChem 10 (2018) 5154–5163.
[22] G.L. Bezemer, P.B. Radstake, U. Falke, H. Oosterbeek, H.P.C.E. Kuipers, A.J. van Dillen, K.P. de Jong, Investigation of promoter effects of manganese oxide on carbon nanofiber-supported cobalt catalysts for Fischer-Tropsch synthesis, J. Catal. 237 (2006) 152–161.
[23] J.P. Den Breejen, A.M. Frey, J. Yang, A. Holmen, M.M. van Schooneveld, F.M.F. de Groot, O. Stephan, J.H. Bitter, K.P. de Jong, A highly active and selective manganese oxide promoted cobalt-on-silica Fischer-Tropsch catalyst, Top. Catal. 54 (2011) 768.
[24] F. Morales, E. de Smit, F.M.F. de Groot, T. Visser, B.M. Weckhuysen, Effects of manganese oxide promoter on the CO and H2 adsorption properties of titania-supported cobalt Fischer-Tropsch catalysts, J. Catal. 246 (2007) 91–99.
[25] Y. Liu, K. Murata, M. Inaba, I. Takahara, Synthesis of ethanol from methanol and syngas through an indirect route containing methanol dehydrogenation, DME carbonylation, and methyl acetate hydrogenolysis, Fuel Process. Technol. 110 (2013) 206–213.
[26] X. Ma, Z. Yang, X. Liu, X. Tan, Q. Ge, Dynamic redox cycle of Cu0 and Cu+ over Cu/SiO2 catalyst in ester hydrogenation, RSC Adv. 5 (2015) 37581–37584.
[27] X. Meng, H. Guo, Q. Wang, Y. Xiao, C. Chen, B. Hou, D. Li, Elucidating the nature and role of copper species in catalytic carbonylation of methanol to methyl acetate over copper/titania–silica mixed oxides, Catal. Sci. Technol. 7 (2017) 3511–3523.
[28] M.A.N. Santiago, M.A. Sanchez-Castillo, R.D. Cortright, J.A. Dumesic, Catalytic reduction of acetic acid, methyl acetate, and ethyl acetate over silica-supported copper, J. Catal. 193 (2000) 16–28.
[29] S. Wang, S. Yin, W. Guo, Y. Liu, L. Zhu, X. Wang, Influence of inlet gas composition on dimethyl ether carbonylation and the subsequent hydrogenation of methyl acetate in two-stage ethanol synthesis, New J. Chem. 40 (2016) 6460–6466.
[30] W. Yue, L. Junyu, Z. Jian, W. Shengping, Z. Yujun, M. Xinbin, Hydrogenation of methyl acetate to ethanol by Cu/ZnO catalyst encapsulated in SBA-15, AlChE J. 63 (2017) 2839–2849.
[31] Y. Zhao, B. Shan, Y. Wang, J. Zhou, S. Wang, X. Ma, An effective CuZn–SiO2 bimetallic catalyst prepared by hydrolysis precipitation method for the hydrogenation of methyl acetate to ethanol, Ind. Eng. Chem. Res. 57 (2018) 4526–4534.
[32] W. Zhou, J. Kang, K. Cheng, S. He, J. Shi, C. Zhou, Q. Zhang, J. Chen, L. Peng, M. Chen, Y. Wang, Direct conversion of syngas into methyl acetate, ethanol, and ethylene by relay catalysis via the intermediate dimethyl ether, Angew. Chem. Int. Ed. 57 (2018) 12012–12016.
[33] H. Yue, Y. Zhao, X. Ma, J. Gong, Ethylene glycol: properties, synthesis, and applications, Chem. Soc. Rev. 41 (2012) 4218–4244.
[34] A.E. Farrell, R.J. Plevin, B.T. Turner, A.D. Jones, M. O'Hare, D.M. Kammen, Ethanol can contribute to energy and environmental goals, Science 311 (2006) 506–508.
[35] J.W. Evans, M.S. Wainwright, N.W. Cant, D.L. Trimm, Structural and reactivity effects in the copper-catalyzed hydrogenolysis of aliphatic esters, J. Catal. 88 (1984) 203–213.
[36] J. Schittkowski, K. Tölle, S. Anke, S. Stürmer, M. Muhler, On the bifunctional nature of Cu/ZrO2 catalysts applied in the hydrogenation of ethyl acetate, J. Catal. 352 (2017) 120–129.
[37] A.K. Agarwal, N.W. Cant, M.S. Wainwright, D.L. Trimm, Catalytic hydrogenolysis of esters: a comparative study of the reactions of simple formates and acetates over copper on silica, J. Mol. Catal. 43 (1987) 79–92.
[38] R. Beerthuis, J.W. de Rijk, J.M.S. Deeley, G.J. Sunley, K.P. de Jong, P.E. de Jongh, Particle size effects in copper-catalyzed hydrogenation of ethyl acetate, J. Catal. 388 (2020) 30–37.
[39] A.L. Patterson, The Scherrer formula for X-ray particle size determination, Phys. Rev. 56 (1939) 978–982.
[40] B. Ravel, M. Newville, ATHENA, ARTEMIS, HEPHAESTUS: data analysis for X-ray absorption spectroscopy using IFEFFIT, J. Synchrotron Radiation 12 (2005) 537–541.
[41] H.H. Kung, Deactivation of methanol synthesis catalysts - a review, Catal. Today 11 (1992) 443–453.
[42] M.B. Fichtl, D. Schlereth, N. Jacobsen, I. Kasatkin, J. Schumann, M. Behrens, R. Schlögl, O. Hinrichsen, Kinetics of deactivation on Cu/ZnO/Al2O3 methanol synthesis catalysts, Appl. Catal. A 502 (2015) 262–270.
[43] G. Prieto, J. Zečević, H. Friedrich, K.P. de Jong, P.E. de Jongh, Towards stable catalysts by controlling collective properties of supported metal nanoparticles, Nat. Mater. 12 (2013) 34–39.
[44] Y. Wang, J. Liao, J. Zhang, S. Wang, Y. Zhao, X. Ma, Hydrogenation of methyl acetate to ethanol by Cu/ZnO catalyst encapsulated in SBA-15, AlChE J. 63 (2017) 2839–2849.
[45] Z. Lu, H. Yin, A. Wang, J. Hu, W. Xue, H. Yin, S. Liu, Hydrogenation of ethyl acetate to ethanol over Cu/ZnO/MOx (MOx=SiO2, Al2O3, and ZrO2) catalysts, J. Ind. Eng. Chem. 37 (2016) 208–215.
[46] R. Van den Berg, T.E. Parmentier, C.F. Elkjaer, C.J. Gommes, J. Sehested, S. Helveg, P.E. de Jongh, K.P. de Jong, Support functionalization to retard ostwald ripening in copper methanol synthesis catalysts, ACS Catal. 5 (2015) 4439–4448.
[47] R. Van den Berg, G. Prieto, G. Korpershoek, L.I. van der Wal, A.J. van Bunningen, S. Lægsgaard-Jørgensen, P.E. de Jongh, K.P. de Jong, Structure sensitivity of Cu and CuZn catalysts relevant to industrial methanol synthesis, Nat. Commun. 7 (2016) 13057.
[48] G. Wang, R. van den Berg, C. de Mello Donega, K.P. de Jong, P.E. de Jongh, Silica-supported Cu2O nanoparticles with tunable size for sustainable hydrogen generation, Appl. Catal. B 192 (2016) 199–207.
[49] C.E. Pompe, M. Slagter, P.E. de Jongh, K.P. de Jong, Impact of heterogeneities in silica-supported copper catalysts on their stability for methanol synthesis, J. Catal. 365 (2018) 1–9.
[50] A. Dandekar, R.T.K. Baker, M.A. Vannice, Carbon-supported copper catalysts, J. Catal. 184 (1999) 421–439.
[51] E.R. Stobbe, B.A. de Boer, J.W. Geus, The reduction and oxidation behaviour of manganese oxides, Catal. Today 47 (1999) 161–167.
[52] S. Lomate, A. Sultana, T. Fujitani, Effect of SiO2 support properties on the performance of Cu-SiO2 catalysts for the hydrogenation of levulinic acid to gamma valerolactone using formic acid as a hydrogen source, Catal. Sci. Technol. 7 (2017) 3073–3083.
[53] A.I. Frenkel, C.W. Hills, R.G. Nuzzo, A view from the inside: complexity in the atomic scale ordering of supported metal nanoparticles, J. Phys. Chem. B 105 (2001) 12689–12703.
[54] J. de Graaf, A.J. van Dillen, K.P. de Jong, D.C. Koningsberger, Preparation of highly dispersed Pt particles in zeolite Y with a narrow particle size

distribution: characterization by hydrogen chemisorption, TEM, EXAFS spectroscopy, and particle modeling, J. Catal. 203 (2001) 307–321.
[55] J.T. Miller, A.J. Kropf, Y. Zha, J.R. Regalbuto, L. Delannoy, C. Louis, E. Bus, J.A. van Bokhoven, The effect of gold particle size on AuAu bond length and reactivity toward oxygen in supported catalysts, J. Catal. 240 (2006) 222–234.
[56] T. Popa, Y. Zhang, E. Jin, M. Fan, An environmentally benign and low-cost approach to synthesis of thermally stable industrial catalyst Cu/SiO2 for the hydrogenation of dimethyl oxalate to ethylene glycol, Appl. Catal. A 505 (2015) 52–61.
[57] M.V. Twigg, M.S. Spencer, Deactivation of supported copper metal catalysts for hydrogenation reactions, Appl. Catal. A 212 (2001) 161–174.
[58] Z. He, H. Lin, P. He, Y. Yuan, Effect of boric oxide doping on the stability and activity of a Cu–SiO2 catalyst for vapor-phase hydrogenation of dimethyl oxalate to ethylene glycol, J. Catal. 277 (2011) 54–63.
[59] C.-L. Ye, C.-L. Guo, J.-L. Zhang, Highly active and stable CeO2–SiO2 supported Cu catalysts for the hydrogenation of methyl acetate to ethanol, Fuel Process. Technol. 143 (2016) 219–224.